PAPER

Towards understanding ELM mitigation: the effect of axisymmetric lobe structures near the X-point on ELM stability

To cite this article: I.T. Chapman *et al* 2012 *Nucl. Fusion* **52** 123006

IOP Publishing and International Atomic Energy Agency Nuclear Fusion
Nucl. Fusion **52** (2012) 123006 (12pp) doi:10.1088/0029-5515/52/12/123006

Towards understanding ELM mitigation: the effect of axisymmetric lobe structures near the X-point on ELM stability

I.T. Chapman, A. Kirk, S. Saarelma, J.R. Harrison, R. Scannell and the MAST Team

Euratom/CCFE Fusion Association, Culham Science Centre, Abingdon, OX14 3DB, UK

E-mail: ian.chapman@ccfe.ac.uk

Received 19 June 2012, in final form 5 October 2012
Published 6 November 2012
Online at stacks.iop.org/NF/52/123006

Abstract
The application of resonant magnetic perturbations (RMPs) with toroidal mode number $n = 4$ or $n = 6$ is observed to result in a significant increase in ELM frequency, despite a reduction in the edge pressure gradient. A picture for how type-I ELMs are mitigated, or destabilized, when magnetic perturbations are applied is proposed. Despite the magnetic perturbation incurring a drop in the pedestal pressure gradient, the critical pressure for an ELM to be triggered is dropped even further. Various mechanisms which could cause this degradation of the stability boundary are outlined. The stability of the edge of MAST H-mode plasmas has been tested when lobe structures are present in the separatrix after application of RMPs. The axisymmetric stability analysis presented here shows that when the plasma boundary is simulated with a model for the observed lobe structures included, the ballooning stability is degraded. This degradation in ballooning stability originates from the perturbed field lines dwelling in the region of unfavourable curvature due to the presence of lobe structures rather than the change in the plasma boundary shape.

(Some figures may appear in colour only in the online journal)

1. Introduction

When tokamak plasmas operate in a high-confinement regime, they are usually susceptible to explosive, quasi-periodic instabilities called edge-localized modes (ELMs) [1]. Type-I ELMs are understood to be a manifestation of so-called peeling–ballooning instabilities driven by strong pressure gradients and localized current density at the edge of the plasma [2, 3]. Whilst it is desirable to operate tokamak plasmas with high confinement, the resultant ELMs can eject large amounts of energy and particles from the confined region, which in turn could result in damage to plasma facing components [4]. In order to avoid damage to the vessel components in future tokamaks like ITER, a robust ELM control scheme is required to suppress the ELMs completely or, at least, to reduce their size by at least an order of magnitude [5]. One such actuator, presently under consideration for ITER, is the application of resonant magnetic perturbations (RMPs), which perturb the local magnetic field in the pedestal region at the edge of the confined plasma. RMPs have been applied to completely suppress ELMs in DIII-D [6, 7], or to mitigate ELMs—that is to say increase their frequency and reduce their amplitude—in ASDEX Upgrade [8], MAST [9] and JET [10].

The most widely offered explanation for ELM suppression is that the application of RMPs induces a stochastic magnetic field giving rise to enhanced heat and particle transport, which in turn degrades the pressure gradient in the pedestal to below the level required to trigger an ELM [6]. Recently it has been postulated that the presence of a magnetic island near the pedestal top acts to prevent the widening of the pedestal and stop the plasma reaching the conventional peeling–ballooning magnetohydrodynamic (MHD) stability boundary [11]. However, the increase in type-I ELM frequency, that is to say *destabilization* of ELMs, when RMPs are applied cannot be explained through this mechanism. Stability analyses of plasmas exhibiting ELM mitigation under the application of RMPs typically find that the peeling–ballooning stability margin is considerably enhanced [12], contrary to the increase in ELM frequency observed. Understanding this dichotomy in the empirical effect of RMPs—either a stabilization of the ELMs by reducing the pressure gradient or a marked destabilization despite a reduction in pressure gradient—is key to understanding how RMPs control ELMs. If one accepts the model of stochastization and subsequent reduction in the pressure gradient as a mechanism for achieving ELM suppression, a satisfactory model must also explain how a

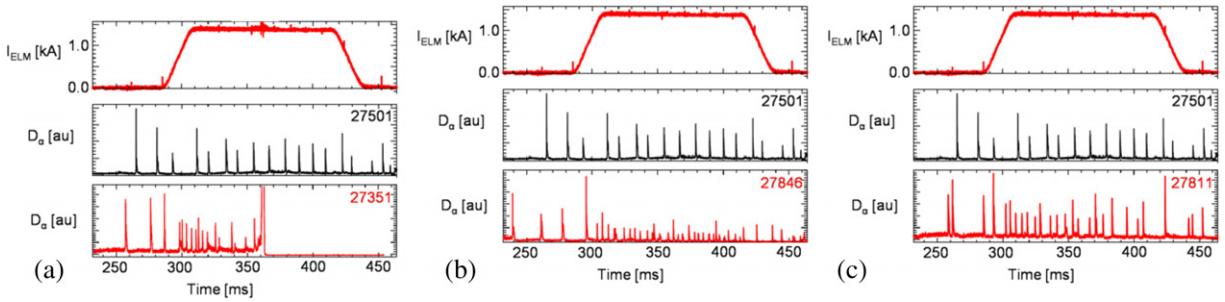

Figure 1. The time traces of the coil current in the ELM control coils and the divertor D_α intensity without and with RMPs applied for (*a*) discharge 27351 with $n = 3$ RMP, (*b*) discharge 27846 with $n = 4$ RMP and (*c*) discharge 27811 with $n = 6$ RMP all compared with the same type of lower single-null MAST plasma from shot 27501 without RMPs.

destabilization of ELMs occurs when the same applied RMP is slightly off-resonance, but yet still causes a reduction in the pedestal density gradient [7].

In an ideal axisymmetric diverted magnetic configuration, the separatrix, or last closed flux surface (LCFS), separates the closed field-lines that confine the plasma, and the open field-lines. The application of non-axisymmetric RMPs has been predicted to cause a deformation of the separatrix, which can lead to significantly radially extended structures near to the X-point [13, 14]. This deformation of the separatrix was recently observed for the first time using visible-light imaging on MAST [15]. In order to consider whether the observed lobes may shed new light on the ELM mitigation (i.e. destabilization) mechanism, we first present brief experimental observation of the effect of RMPs on MAST plasmas in section 2. This gives rise to a picture for how ELM mitigation may occur described in section 3 stimulated by the experimental observation of lobes near the X-point. One conjecture is that the presence of the lobes near the poloidal field null destabilize the peeling–ballooning modes since the field-lines spend a larger proportion of their trajectory in a region of unfavourbale curvature. In order to investigate this, the reconstruction of axisymmetric equilibria with lobe structures in the poloidal cross-section is discussed in section 4 before the implications for linear peeling–ballooning stability are assessed numerically in section 5. Conclusions and implication of this work for RMP ELM control in ITER are discussed in section 6.

2. Effect of applied fields on ELMs and plasma shape

MAST is equipped with 18 in-vessel ELM control coils. The internal coils are constructed from an aluminium alloy and are composed of four turns each designed to carry currents up to 2 kA/turn (although the present power supplies are limited to 1.4 kA). The coils measure 270 mm poloidally by 600 mm toroidally and are arranged in two equally spaced toroidal rows, one above the midplane containing six coils and one below the midplane comprising twelve coils. This flexible coil set allows the application of $n = 3, 4, 6$ fields, where n is the toroidal periodicity. The effect of applying perturbations with different toroidal mode number has been investigated in MAST single-null diverted (SND) plasmas. These vertically down-shifted plasmas feel the applied field predominantly from the lower row of coils only.

The application of both $n = 4$ and $n = 6$ RMPs results in a significant increase in type-I ELM frequency, and a reduction in the energy lost per ELM [15]. Figure 1 shows the divertor D_α emission intensity in identical plasmas with $n = 3$, $n = 4$ and $n = 6$ applied fields, compared with a shot without applied RMPs. It is clear that the application of $n = 4$ RMPs results in an increase in ELM frequency of a factor of three, whilst $n = 6$ RMPs increase the ELM frequency by a factor of two, and both with commensurate drops in the energy lost per ELM. This is typical of the effect of high-n RMPs on ELM behaviour, where ELM mitigation is routinely observed in MAST, and indeed, the increase in ELM frequency can be much higher when the plasmas are optimized for this by changes to the q-profile to optimize the resonance and moving the plasma closer to the in-vessel coils. Meanwhile, the application of $n = 3$ RMPs causes global plasma braking, short-lived back transitions to the low-confinement regime, then eventually locks the plasma and induces a disruption (though it is worth noting that $n = 3$ RMPs do mitigate type-I ELMs in other MAST scenarios).

During the SND discharges shown in figure 1, the lower X-point region has been imaged using a toroidally viewing camera with spatial resolution of 1.8 mm in the tangency plane, filtered with either a He II (468 nm) or C III (465 nm) filter and using a 300 μs integration time. Figure 2 shows false colour images obtained with the He II filter during an inter-ELM period when $n = 3, 4, 6$ RMPs are applied to a MAST SND H-mode. A deformation of the separatrix is observed and clear lobe structures can be seen near to the X-point. The location, radial extent and poloidal separation of the lobes are different for each toroidal mode number of the applied field. Furthermore, the position of the lobes is dependent upon the phase of the applied field relative to the toroidal location of the camera tangency plane. The lobe structures are only observed above a critical applied field threshold, which is consistent with the necessary magnetic perturbation required to affect the plasma, that is to say, for enhanced particle transport, or density pump-out, to be observed in L-mode or for an increase in ELM frequency to be observed in H-mode.

The pedestal profile evolution when RMPs are applied is diagnosed using MAST's Thomson scattering system which measures the electron temperature and density with a spatial resolution better than 10 mm on both the high- and low-field sides of the plasma. When the RMPs are applied, the pedestal pressure gradient is degraded whilst the pedestal width increases [19]. Figure 3 shows the electron pressure profile at approximately 80% through an ELM cycle, as measured by

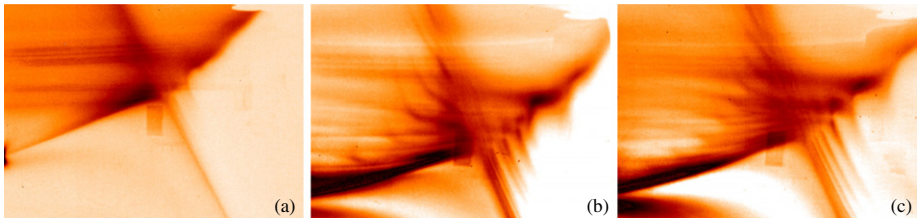

Figure 2. False colour images captured by high-speed visible camera during an inter-ELM period of H-mode when (*a*) $n = 3$, (*b*) $n = 4$ and (*c*) $n = 6$ RMPs are applied.

the Thomson scattering diagnostic for two identical MAST discharges with and without an applied $n = 6$ field. This increase in the pedestal width and reduction in the pressure gradient is regularly observed in MAST plasmas when ELM mitigation is observed, and is discussed in more detail in [19]. It is worth noting that figure 3 shows that the RMPs cause a displacement of the edge of the plasma by a few centimetres—this three-dimensional distortion of the plasma is likely to be important in determining ELM stability.

Whilst the increase in the pedestal width does induce a drop in the critical pressure gradient required for peeling–ballooning instability [20], the degraded pressure gradient is significantly below the critical threshold, and so the application of RMPs of all toroidal mode numbers enhances stability. This is demonstrated in figure 4, where the stability boundary for a MAST discharge with $n = 6$ RMPs applied is illustrated. This stability diagram is constructed by reconstructing the experimental equilibrium and systematically varying the edge pressure gradient and current density around this experimental point. For each normalized pressure gradient, α, and current density, j, a new equilibrium is created with the HELENA code [21] and its stability to various finite-n peeling–ballooning modes is tested using the ELITE code [2, 22]. This method is described in detail in [23]. Here the plasma shape is taken from EFIT reconstruction and held fixed (note that the X-point is slightly smoothed to avoid numerical problems), whilst the electron temperature and density profiles are taken from Thomson scattering measurements before and after the application of RMPs. The ion temperature is assumed to be equal to the electron temperature. Whilst this assumption may be invalid, assuming a flat ion temperature in the pedestal instead has been shown to have little effect on the stability boundary [20]. The edge current density is found from a self-consistent bootstrap current iterative calculation constrained by the total plasma current, using the formulae from [24, 25]. Having tested finite-n linear stability for $n = 5, 10, 15, 20, 25, 30$ a stability boundary is drawn in this $[j, \alpha]$ space, as illustrated in figure 4. Here, the normalized pressure is defined as

$$\alpha = -\frac{2\partial V/\partial\psi}{4\pi^2}\left(\frac{V}{2\pi^2 R_0}\right)^{1/2}\mu_0\frac{\partial p}{\partial\psi} \qquad (1)$$

where V is the volume enclosed by flux surface with poloidal flux, ψ, p is the pressure and R_0 is the major radius of the geometrical plasma centre. It is clear that when an $n = 6$ RMP is applied, the decrease in the observed pressure gradient is expected to make the plasma more stable to finite-n peeling–ballooning modes, whilst figure 1 clearly shows the type-I ELMs are destabilized and more frequent. The wider pedestal means that the ballooning stability boundary moves to lower normalized pressures since a lower-n mode can become unstable with a wider transport barrier. Indeed, the toroidal mode number of the limiting peeling–ballooning mode—i.e. that found at the corner with maximum pressure and current—drops from $n = 25$ before the RMP is applied to $n = 20$ for the wider pressure pedestal after application of the RMP. Incidentally, this gives confidence that a sufficient scan in toroidal mode number has been performed to find the stability boundary when the RMP is applied. Despite the reduction in α of the stability boundary, the measured pressure gradient drops significantly further than the critical α afforded by the destabilization caused by widening of the pedestal, and thus the plasma is expected to be within the stable region.

3. Modelling the effect of local lobes near the X-point and the implications for ELM mitigation by RMPs

The fact that the reduced pressure gradient is predicted to be well inside the peeling–ballooning stability boundary, yet the ELM frequency *increases* implies that either (i) the peeling–ballooning model no longer applies, (ii) another effect increases the pressure gradient in the pedestal, for instance fast ion redistribution not measured by electron temperature diagnostics, or (iii) the stability boundary is degraded from that shown in figure 4. A picture for how ELM mitigation, i.e. a destabilization of ELMs, occurs when RMPs are applied is stimulated by the experimental results in section 2. The peeling–ballooning trigger for an ELM is now widely accepted after numerous empirical studies have shown excellent accordance with numerical analysis. In the model suggested here, the mitigated frequent ELMs remain a manifestation of peeling–ballooning modes when the ideal MHD stability boundary is crossed. The effect of the RMP is to reduce the critical pressure gradient at which a peeling–ballooning mode is destabilized, below the level to which the enhanced particle transport drops the pedestal gradient. This concept is illustrated in a cartoon in figure 5. As well as dropping the pressure gradient, the RMPs have various effects which could cause the degradation of the stability boundary: (1) the deformation of the plasma shape which influences ballooning stability; (2) a change in the edge rotation shear [26–28], which is known to stabilize peeling–ballooning modes [29], and therefore any variation in the rotation profile is likely to affect stability and could trigger ELMs; (3) the toroidal periodicity [30], since it has been shown that ballooning modes can be more unstable in local toroidal positions when the plasma is non-axisymmetric [31–33]; or (4) field-lines dwelling in the unfavourable curvature region due

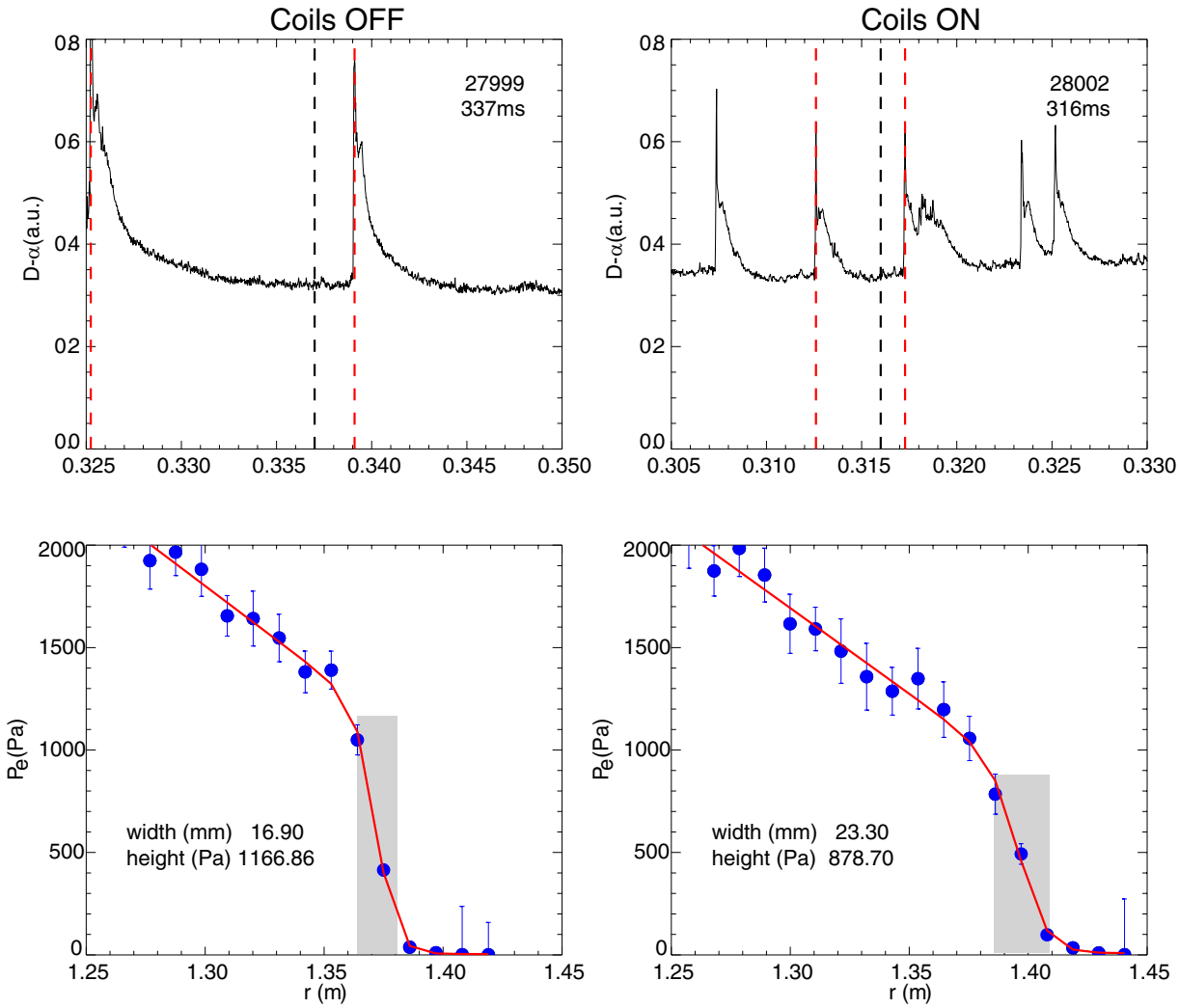

Figure 3. The radial electron pressure profile in the pedestal as measured by the Thomson scattering diagnostic time for MAST shot 28002 when an $n = 6$ RMP is applied compared with 27999 when there is no applied magnetic perturbation. The profiles are taken at approximately 80% of the inter-ELM period, indicated by the vertical dashed line between the lines demarking the ELM period.

to the presence of lobe structures near the X-point. This means that a peeling–ballooning mode requires a lower pressure gradient to become linearly unstable when RMPs are applied. There exists an operating regime when the RMP does not incur sufficient drop in the pressure gradient to go below the new, lowered stability boundary, and so the ELMs become more frequent. There is no reason per se that suppression requires a stronger degradation of the ballooning stability boundary; indeed, perhaps the optimal situation is one whereby there is only a small degradation in ballooning stability, but sufficient pedestal transport that the pedestal will never reach this degraded stability boundary. In this paper, we consider the effect of field-lines dwelling in the unfavourable curvature region near the X-point has on the stability boundary by changing the axisymmetric plasma cross-section.

4. Plasma equilibrium with lobe structures

The lobe structures observed when RMPs are applied, as seen clearly in figure 2, were predicted as manifestations of the homoclinic tangle which replaces the separatrix when the magnetic field is perturbed [13]. Non-axisymmetric magnetic perturbations were predicted to split the separatrix into stable and unstable manifolds [14], with corrugated structures forming where these manifolds intersect. These homoclinic tangles are computed to be particularly complex and extended near the X-point. This concept of lobe structures formed by the invariant manifolds of the perturbed field has been used to explain the splitting of the divertor leg footprints observed on strike-point targets during RMP experiments [34–36]. Furthermore, the predictions of the number, location and separation of the lobe structures from vacuum field-line tracing agrees well with those observed in the camera images [15]. If one believes that RMPs cause complete stochastization of the magnetic field in the pedestal region (and it is predicted in [37] that the radial extent of the lobes outwards sets a minimum value on the radial extent of the stochastic layer in the plasma), then any equilibrium and stability analysis based upon nested flux surfaces is a flawed representation of reality. Nonetheless, due to complexity of modelling a resistive, three-dimensional plasma, this is routine practice [7, 12, 38, 39]. It should be noted that ideal MHD analysis with RMPs predicts that the

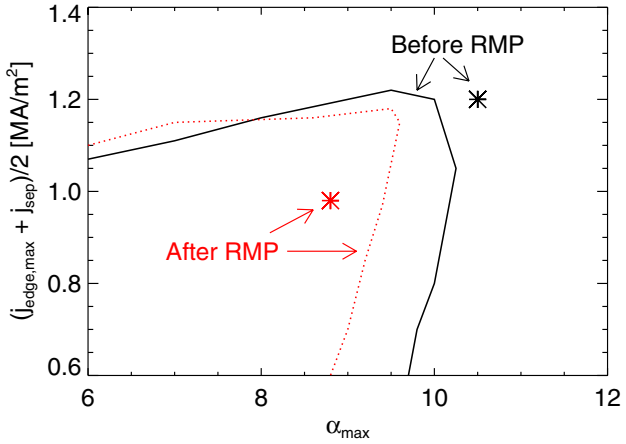

Figure 4. The edge stability diagram constructing by varying edge pressure, α and current density, j and reconstructing many different equilibria and testing stability to $n = 5, 10, 15, 25, 30$ modes. The stability boundary is assessed when the mode growth rate drops below $\gamma/\omega_A = 0.01$. The star represents the experimental equilibria.

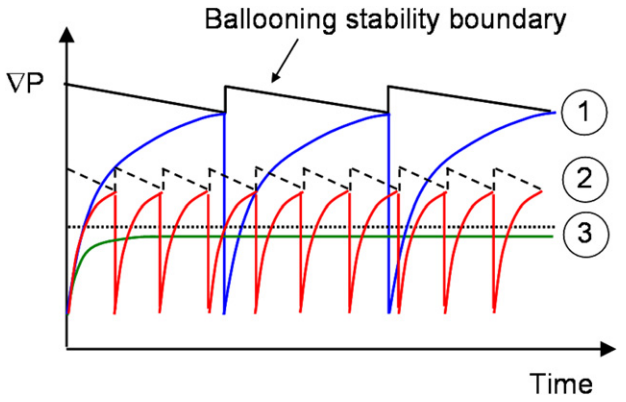

Figure 5. A cartoon of the effect of lobe structures on ELM stability. (1) A typical type-I ELM cycle: the critical pressure gradient for triggering the limiting finite-n peeling–ballooning mode slightly drops during the ELM cycle as the pedestal broadens and current density increases, and eventually is exceeded leading to an ELM crash. (2) ELM mitigation: when an RMP is applied below the critical value for suppression, or off-resonance, the finite-n peeling–ballooning stability limit is degraded. Further, the enhanced infinite-n instability results in an accelerated broadening of the pedestal, which results in a more rapid drop in the critical pressure gradient. Quickly the pressure pedestal exceeds this lower limit and the ELM frequency is much increased. (3) ELM suppression: if the RMP amplitude is increased further or alignment is improved, the particle transport increases so much that the pressure gradient remains below the finite-n peeling–ballooning stability limit.

RMP field gives rise to a significant plasma displacement near the X-point as well, in this case assuming ideal nested flux surfaces [40]. If the lobes are a manifestation of this plasma response to the applied field rather than through ergodization, then the ideal treatment followed here is valid.

Figure 6 shows a laminar plot of the lobe structures when an $n = 6$ RMP is superimposed on the equilibrium plasma, as generated by the ERGOS vacuum field-line tracing code [41]. The poloidal cross-section in figure 6 shows the location of each field-line at a given toroidal location. Each field-line is traced for 200 toroidal turns or until they reach the divertor target. Whilst only field-lines with long connection length

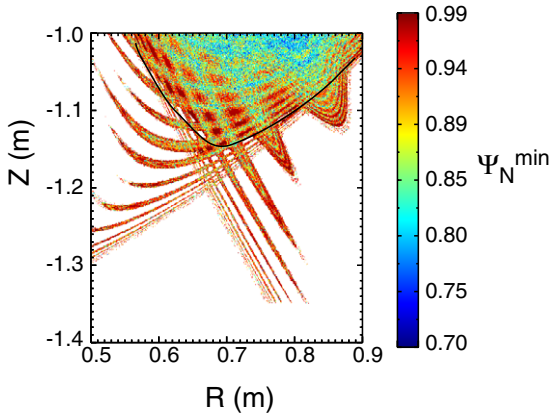

Figure 6. A laminar plot from ERGOS calculations showing the minimum normalized flux experienced by each field-line traced from each given poloidal position in one toroidal plane. The field-lines are followed for 200 toroidal turns or until they reach the divertor target. The black line shows the position of the separatrix with no applied RMPs for comparison.

influence the plasma stability, as discussed later, approximately the same lobe structures are seen for a laminar plot retaining only long connection-length field-lines. They are coloured by the minimum normalized flux that the field-line experiences during its trajectory. It is clear that there are bands in the lobe structures, especially at small radial extent of the lobes. This indicates that even in the ergodized field when RMPs are applied, there is some structure to the field at least away from the lobe periphery. This gives some justification to employing a nested flux surface approximation with lobes in the poloidal shape provided that the lobes are less extended than those predicted by vacuum field-line tracing. In the future non-ideal equilibria allowing for stochastic fields will also be considered. In what follows, we do not consider *how* the lobe structures are formed, merely that we empirically observe that the confined plasma takes this shape, and then assess whether the field-lines dwelling in these lobe structures on the low-field side affects peeling–ballooning stability. Furthermore, it is important to note that we restrict ourselves to distortions to the separatrix that are significantly less radially extended than observed experimentally, which in turn is significantly less extended than the lobes predicted by vacuum field-line tracing calculations. Finally, we also assume axisymmetry in the equilibrium reconstruction, whilst the applied RMPs in MAST cause a non-axisymmetric field. Since we are interested in the effect of field-lines dwelling in the bad curvature region, and the axisymmetric assumption causes this, it partially justifies using this treatment. It should be noted that such a two-dimensional fixed-boundary analysis is strictly invalid though as it neglects the large external currents that would be required in a free boundary calculation to replicate this situation.

4.1. Plasma shape

Reconstructions of MAST equilibria when both $n = 4$ and $n = 6$ RMPs are applied have been performed using the HELENA [21] axisymmetric fixed-boundary, static Grad–Shafranov solver. The plasma shape is taken from the visible-imaging camera, whilst the electron density and temperature

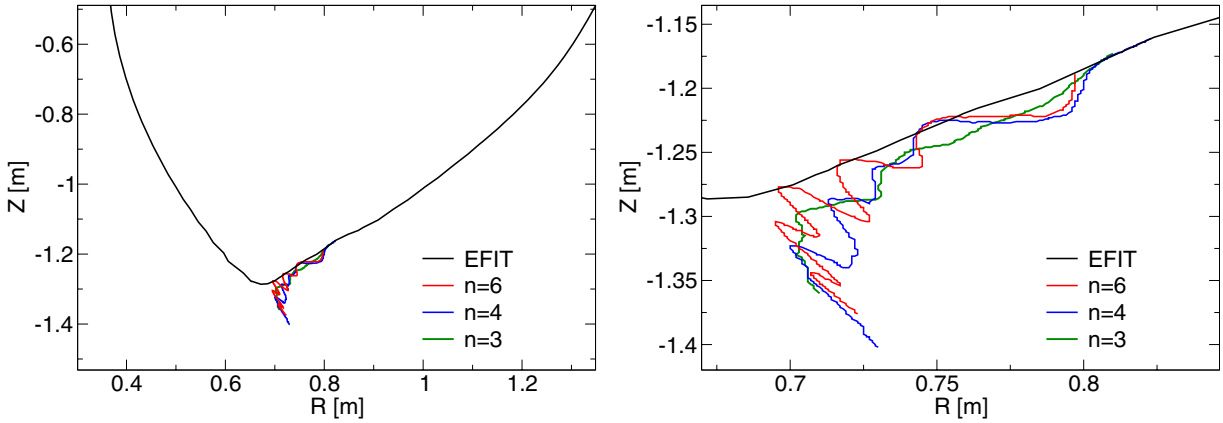

Figure 7. The shape of the plasma separatrix inferred from filtered camera data for MAST discharges with $n = 4$ and $n = 6$ RMPs applied overlaid on the plasma shape predicted by HELENA equilibrium reconstruction. The right figure is a zoomed in view of the left half-plasma cross-section.

profiles are taken from the Thomson scattering data. In order to make the boundary suitable for the HELENA fixed-boundary code, the shape is decomposed into 512 Fourier harmonics, which slightly rounds the lobes. The pedestal profiles are taken before the RMPs are applied, and held fixed throughout. The profiles employed are found to be marginally unstable to $n = 25$ peeling–ballooning modes, as illustrated in figure 4. The increase in the pedestal width and reduction in the pressure gradient illustrated in figure 3 is not considered here, in order that any change in the stability boundary can be attributed directly to the change in the field-line trajectory resultant from the change in the plasma shape.

The lobe structures measured by the camera when $n = 4$ and $n = 6$ RMPs are applied are shown in figure 7. Given the camera position and orientation, each camera pixel can be described by a single line passing through the torus. The Z location is simply calculated from knowing the line trajectory and the distance along the line from the camera to the tangency point, i.e. following the line down in Z to where it is tangent in radius. Here, the LCFS plotted is an emission contour that most closely matches the extent of the plasma within the R, Z plane where the camera pixels are at tangency. Due to the Fourier decomposition of the plasma shape necessitated by the stability codes, we cannot numerically reconstruct an equilibrium with such radially extended and poloidally narrow structures. Therefore, the deformation of the separatrix analysed here is far less severe. However, it is important to note that the change in shape in the axisymmetric treatment employed here is really used as a mechanism for allowing the field-lines to dwell in the region of bad curvature, and as such the actual plasma boundary used is not as important as the fact that lobes are included to mimic this effect. Typical lobe structures that have been analysed when the $n = 4$ and $n = 6$ fields are applied are shown in figure 8. Many equilibria were tested in order to find acceptable shapes which converged numerically for the full range of edge current and pressures needed to find the marginal stability boundary. Figure 8(*a*) shows three different cases of distorted plasma boundaries which have been modelled compared with the shape of the confined plasma measured by the camera when $n = 4$ RMPs are applied. Case 1 has one lobe in the position furthest to the low-field side; case 3 has one narrow lobe in the position nearest to the X-point; and case 2 has two lobes, but with the lobe nearer to the X-point necessarily broadened in order to reach a converged equilibrium. Figure 8(*b*) shows four different plasma shapes compared with the measurement when $n = 6$ RMPs are applied. Case A has one lobe in position marked 'lobe 1', as does case D which has a greater radial extent. Case B has the same 'lobe 1' shape as case A, but with an ancillary lobe in position 'lobe 2'. Case C is an extension of case B to have a third lobe at position 'lobe 3'. Cases B, C and D represent the most extreme configurations possible with lobes in positions 1, 1&2 and 1&2&3, respectively.

Whilst the plasma shape is not perfectly matched to the experimental data, it should be noted that the dominant effect on ballooning stability comes from the field-lines dwelling in the unfavourable curvature region, and thus the change in the poloidal cross-section should be seen as a mechanism to facilitate this effect in the stability analysis, rather than having a direct affect on ELM stability. Case A results in a change in the poloidal field (compared with the shape without lobes) less than the radial field at the lobe position due to applied RMP field. However, case D does require a poloidal field change nearly an order of magnitude larger than the radial field. The sharp lobes result in an increase in the safety factor q near the edge, and a significant increase in the magnetic shear $s = \mathrm{d}q/\mathrm{d}r\, r/q$. The radial profiles of the safety factor and the magnetic shear of the original EFIT smooth boundary equilibrium is compared with two cases with one lobe of different radial extent in figure 9. The two cases with deformed plasma shape correspond to cases A and D from the $n = 6$ shapes illustrated in figure 8(*b*). Both cases have only one lobe in the position furthest to the low-field side, marked as 'lobe 1' in figure 8(*b*). Although the magnetic shear near the boundary increases more than four-fold, the safety factor only increases a little, so any changes in stability are unlikely to be due to q-profile variation.

4.2. *Pedestal evolution*

The pedestal width evolution during an ELM cycle in MAST has been shown [20, 42] to be well described by the concepts underlying the EPED model [43, 44]. Infinite-n ballooning stability has been compared with gyrokinetic analysis and shown to be a good proxy for kinetic ballooning mode stability

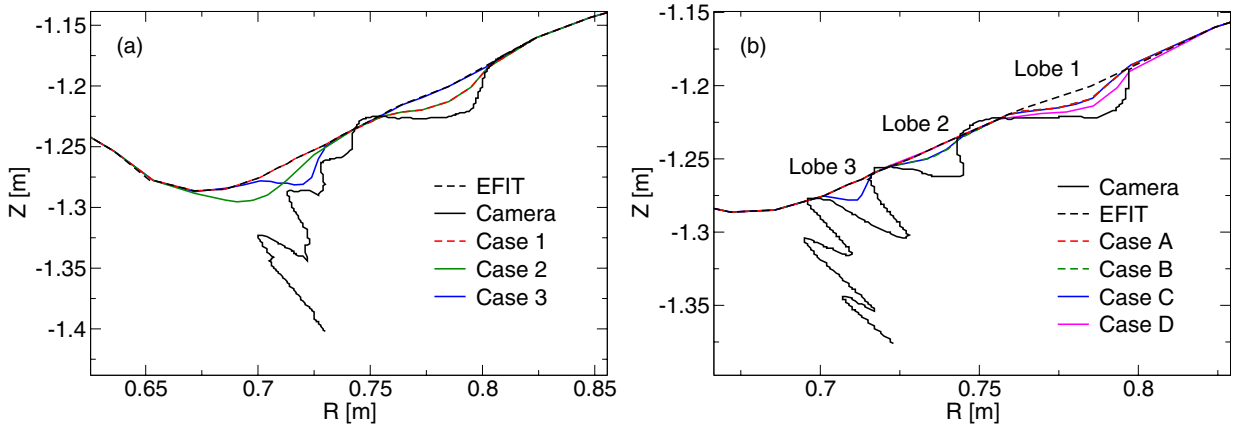

Figure 8. The shape of the plasma boundary used in HELENA reconstruction of MAST plasmas with (left) $n = 4$ RMPs and (right) $n = 6$ RMPs. The different cases have different number, location and radial extent of the lobes. The position and poloidal extent of the lobes is the same as measured by the camera, though the shape and radial extent is constrained by numerical Fourier transformation.

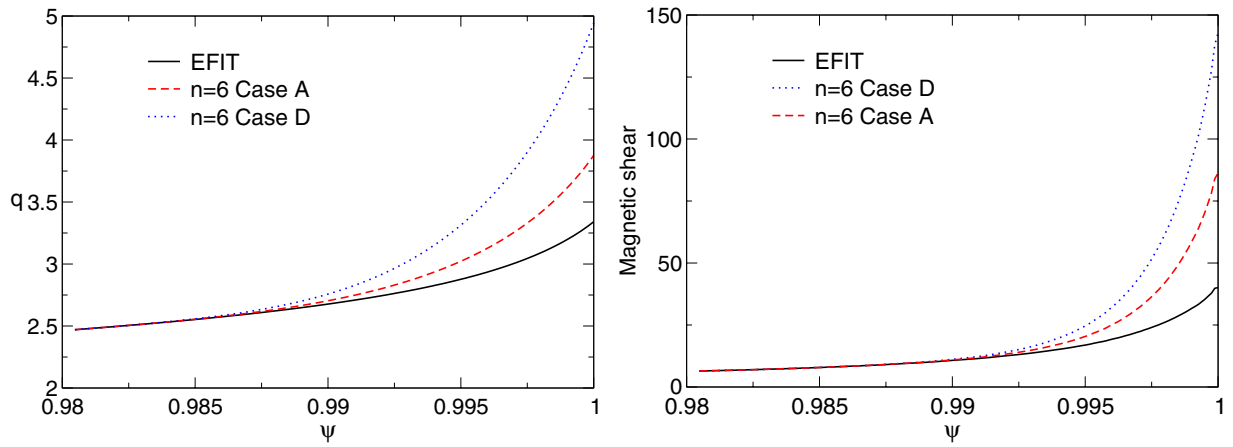

Figure 9. The radial q and magnetic shear profiles near the plasma edge of the original EFIT equilibrium (solid) compared with case A (dashed) and case D (dotted) for one lobe of the $n = 6$ RMP, as shown in figure 8(*b*).

[20]. Figure 3 shows how the application of RMPs typically broadens the pedestal and reduces the maximum pressure gradient. Figure 10 shows the $n = \infty$ ballooning mode stability parameter across the radial extent of the pedestal when the shape is taken from EFIT reconstruction, and when it is assumed to have one lobe, as in case A of figure 8(*b*). Here the infinite-n ballooning stability parameter is defined in [45]. When the ballooning parameter is below unity the infinite-n modes are unstable. The fact that the presence of the lobe exacerbates kinetic ballooning mode instability (assuming infinite-n modes remain a good proxy) suggests that particle transport, assuming a crude gyro-Bohm diffusivity scaling like γ/k^2 (where γ is the growth rate and k is the perpendicular wavenumber), is enhanced, limiting the pressure gradient to a lower value. This is consistent with the pedestal width significantly increasing after the application of RMPs as the pressure gradient is mediated by kinetic ballooning modes. As already discussed in section 2, the broader pedestal width does result in a slightly lower critical pressure gradient for finite-n peeling–ballooning instability. However, the much reduced pressure gradient, which is consistent with the enhanced infinite-n instability shown in figure 10, allows much broader pedestals before the ELM crash. Indeed, as figure 4 shows, in the absence of a destabilization of the finite-n ballooning modes, one might expect a lengthening of the ELM period. We consider whether the presence of the lobes affects this peeling–ballooning stability boundary in section 5.

5. MHD stability in the presence of lobe structures

It is known that introducing an arbitrarily small, radially and poloidally localized bump (used to approximate the effect of an X-point) on the low-field side of tokamak plasmas degrades ballooning stability, whilst vastly enhancing peeling stability [16–18]. Indeed, reference [18] even suggests the idea of using a localized magnetic perturbation to introduce a 'lobe' in the unfavourable curvature region and so trigger ballooning modes. If the X-point is on the low-field side of the torus, then the plasma is more susceptible to ballooning instabilities since the field-lines exist for much of their length in the region of unfavourable curvature ($\langle \kappa \cdot \nabla P \rangle < 0$), whilst approaching the X-point when the poloidal field tends to zero. It is noteworthy that the observed deformation of the separatrix by the presence of the lobes in MAST [15] is considerably larger in radial extent than the small localized deformations studied in [16], or indeed than those studied here, suggesting that these lobe structures

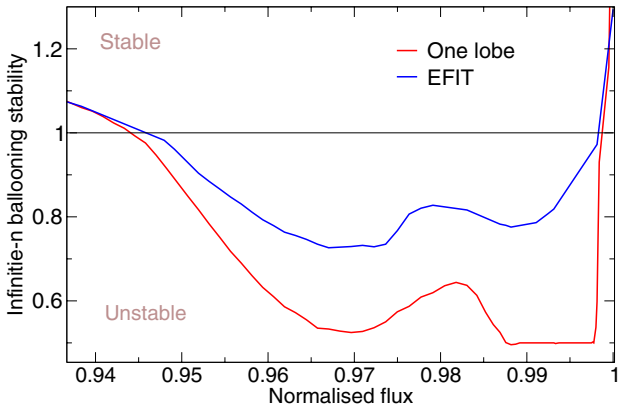

Figure 10. The radial dependence of the infinite-n ballooning stability parameter in the pedestal region for the reconstructed MAST equilibrium with a smooth plasma shape and when one shallow lobe is present. $n = \infty$ ballooning modes, which act as a proxy to kinetic ballooning modes [20], are highly unstable in the presence of a lobe.

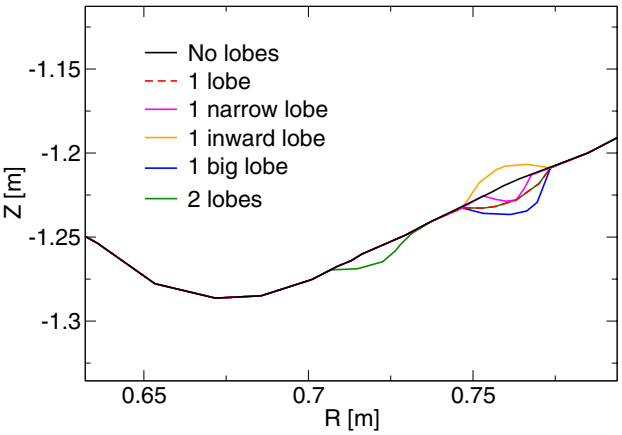

Figure 11. The plasma shape near the X-point for five systematic types of shape deformation similar to the lobes empirically observed.

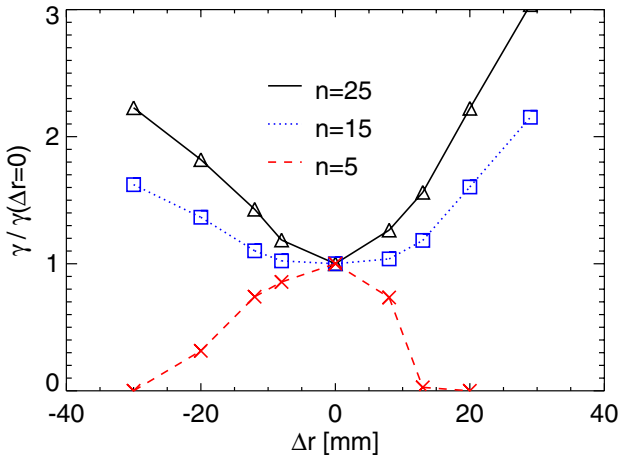

Figure 12. The normalized growth rate of $n = 5, 15, 25$ peeling–ballooning modes for typical MAST profiles and shape with one lobe in an approximate poloidal position as taken from the camera images, but with varying radial extent of the lobe, Δr, and consequently varying time that a given field-line spends in the bad curvature region. Here a negative Δr means the lobe extends into the plasma towards the axis and the mode growth rate is normalized to $\gamma(\Delta r = 0)$.

induced by RMPs are likely to play a significant role in type-I ELM stability.

The stability of the equilibria including lobes, as discussed in section 4, has been tested with the ELITE linear MHD code [2, 22]. In order to reach converged solutions, strong grid packing is required numerically. We employ 400 radial points and 2049 poloidal points, with 100 of the radial points in the final 0.5% of the poloidal flux. Since the codes use straight field-line coordinate systems, the poloidal points are naturally focused in the region of low poloidal field. This is meant as an academic study since an axisymmetric ideal treatment of the plasma is not a true representation of the lobes formed by RMPs, though it is nonetheless useful in stimulating a picture for ELM mitigation.

5.1. Systematic test of the effect of lobe structures

It is well known that locating an X-point on the low-field side of the torus is destabilizing to ballooning modes [12, 46, 47]. The fact that the field-line exists for much of its length near the X-point where the poloidal field is low means that when the X-point is in the unfavourable curvature region on the low-field side, ballooning drive is significantly increased. Conversely, the peeling modes are asymptotically stabilized by the increasing magnetic shear near the X-point [12, 48] irrespective of its poloidal location [12]. Numerically, the inclusion of a sharp lobe on the low-field side in an axisymmetric treatment is tantamount to introducing an X-point since the narrow structure results in a low poloidal field.

In order to gain insight into the radial extent and poloidal width and location of the lobes which have greatest effect on peeling–ballooning stability, a systematic study was performed using an equilibrium with inflated pressure gradient to ensure unstable modes. From references [12, 49] we know that the ballooning stability is progressively degraded the further onto the low-field side the lobe is positioned. Given that the poloidal dependence is known, we take two poloidal positions, consistent with the observed location of the lobes when an $n = 6$ RMP is applied, and vary the depth and width of one lobe and add an ancillary lobe to test the implications for stability. Here we use the radial extent of the lobes as a parameter which affects the extent of field-line dwelling in the unfavourable curvature region, rather than the change in shape directly affecting peeling–ballooning stability. Figure 11 shows some typical lobe shapes grafted onto an EFIT reconstruction of a standard MAST lower SND plasma. The lobes illustrated are the three biggest lobes with this width in these positions which resulted in a converged equilibrium. The lobe furthest from the X-point could be slightly deeper because the Fourier transform requires monotony in the poloidal angle, and this is a stronger constraint for lobes near the X-point as the lobe extremum falls in the shadow of a direct line from the geometrical axis.

Figure 12 shows the growth rate of $n = 5, 15, 25$ peeling–ballooning modes as the radial extent, Δr, of the lobe furthest to the low-field side in figure 11 is varied, and consequently the time that a field-line experiences the unfavourable curvature region during its trajectory changes. The equilibrium has typical MAST profiles, with a significant pressure pedestal and

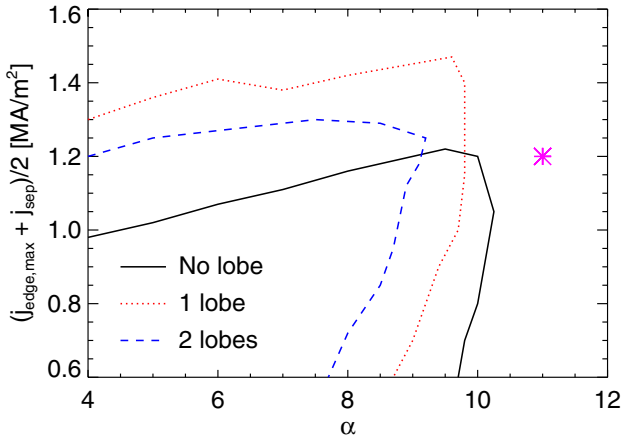

Figure 13. The edge stability diagram constructing by varying edge pressure, α and current density, j and reconstructing many different equilibria and testing stability to $n = 5, 10, 15, 25, 30$ modes. The stability boundary is assessed when the mode growth rate drops below $\gamma/\omega_A = 0.01$ for three different plasma shapes. The rounded shape from EFIT equilibrium reconstruction shows the pedestal is marginally peeling–ballooning unstable at the top corner of operating space. The presence of one big lobe leads to the peeling boundary appearing at increased current density, whilst the ballooning boundary moving to lower pressure gradient, suggesting the operating point would be more unstable. The presence of two lobes (with smaller radial extent) has less affect on the peeling mode, but is even more destabilizing to the ballooning modes, moving the plasma profiles even further into the unstable region. The star represents the typical experimental equilibrium from which the starting pedestal profiles were taken.

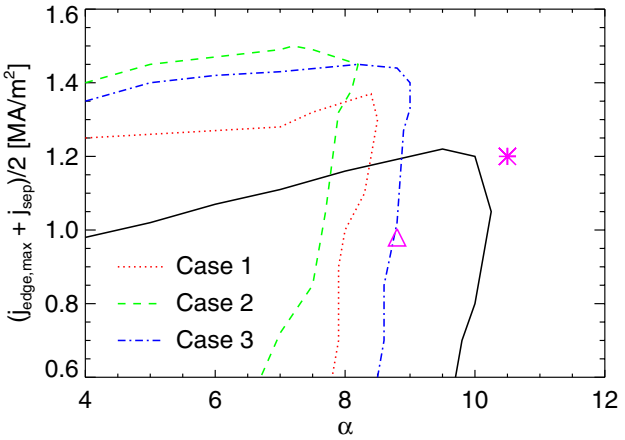

Figure 14. The finite-n peeling–ballooning stability boundary for a MAST single-null plasma when an $n = 4$ RMP is applied and the plasma shape is taken as the boundaries illustrated in figure 8(a). The star represents the experimental equilibria before applying the $n = 4$ RMP, and the triangle is the experimental point after applying the perturbation.

bootstrap current near the edge. As the lobe extent increases, the high-n peeling–ballooning mode is strongly destabilized, consistent with the field-lines experiencing the bad curvature region for longer. Even at $n = 15$, the dominantly ballooning character of the mode means that an increase in lobe extent results in a more unstable mode. Conversely, the $n = 5$ mode is stabilized by the increase in lobe extent. This happens at low toroidal mode number where the mode is dominantly peeling in character since the strong increase in the edge magnetic shear, as discussed in section 4, stabilizes the peeling mode. When the lobe extends into the plasma rather than protruding outwards (here defined as negative Δr), the stability of the peeling–ballooning modes are affected in the same way, but with decreased sensitivity. This is because the magnetic shear affecting the peeling modes and the change in the curvature affecting the ballooning modes is less pronounced for an inward lobe. At intermediate-n, the lobes have little effect on the growth rate of the mode as the increase in the magnetic shear stabilizes the peeling drive, counteracting the destabilization of the ballooning component by the increased curvature. The presence of the lobes changes the mode eigenfunction to be more ballooning in character, which is to say that the displacement becomes less edge localized—an effect described in detail and illustrated in [16].

The addition of an ancillary lobe has also been tested using ELITE stability analysis and is illustrated in figure 13. Perhaps unsurprisingly, adding an extra lobe with the same radial extent destabilizes the ballooning modes more than just a solitary lobe. Adding a second lobe increases the magnetic shear even more and naturally results in field-lines spending more time in the unfavourable curvature region. Interestingly, the addition of the second lobe makes the plasma more ballooning unstable than one lobe with greater radial extent. Whilst the two small lobes do not increase the magnetic shear as much as one more extended lobe, so the peeling boundary occurs at lower edge current density, they do have a more destabilizing effect on the ballooning boundary. This suggests that provided the RMPs result in lobes of sufficient extent, it is more important to have multiple lobes than just one with a larger perturbation in order to optimize ELM mitigation.

5.2. Modelling of MAST plasma stability in the presence of lobe structures

The equilibrium reconstruction with fixed-boundary representation of the plasma shape necessary for the stability analysis precludes using a shape with very extended lobe structures as seen by the camera and shown in figure 7. However, the stability boundary has been tested for MAST single-null plasmas with $n = 3, 4, 6$ RMPs applied using the shapes illustrated in figure 8. The poloidal width and location of the lobes matches that seen in the visible imaging, but the radial extent is necessarily smaller. Throughout the scans, the pedestal width is assumed to be that before the RMPs are applied. As figure 4 shows, if the pedestal width in the stability analysis is increased to that measured by the Thomson scattering diagnostic, then the ballooning stability boundary moves to lower pressure. This effect would therefore be in addition to changes to the stability boundary reported in this section. It is worth noting that as well as the inability to model the full radial extent, the lobes are only measured in one toroidal location, whereas vacuum field-line tracing would predict different lobe patterns at different toroidal locations, so the change in stability presented here is a qualitative representation of the effect of the RMP.

Firstly we consider the effect of the lobe structures present when an $n = 4$ RMP is applied. Figure 14 shows the peeling–ballooning stability boundary from ELITE linear simulations when the three shapes illustrated in figure 8(a) have been

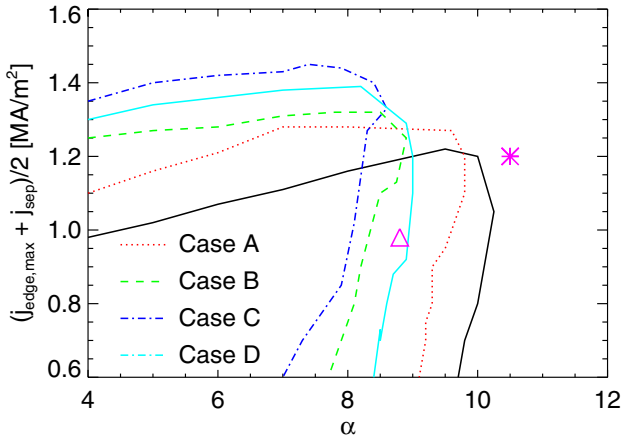

Figure 15. The finite-n peeling–ballooning stability boundary for a MAST single-null plasma when an $n = 6$ RMP is applied and the plasma shape is taken as the boundaries illustrated in figure 8(b). The star represents the experimental equilibria before applying the $n = 6$ RMP, and the triangle is the experimental point after applying the perturbation.

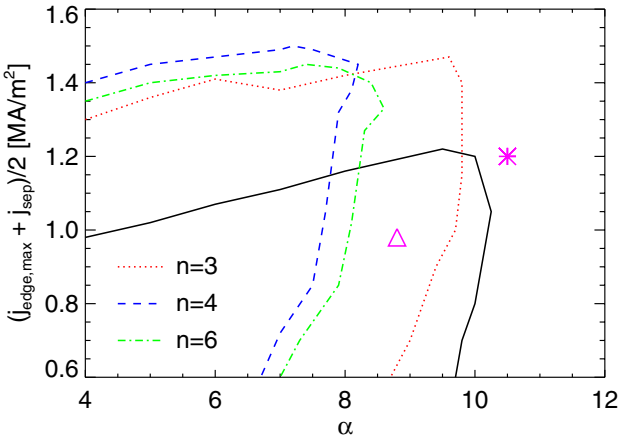

Figure 16. The finite-n peeling–ballooning stability boundary for a MAST single-null plasma when an $n = 6$ RMP is applied and the plasma shape is taken as the boundaries taken as case 2 from figure 8(a) for $n = 4$ and case C from figure 8(b) for $n = 6$ with the $n = 3$ matching well to the camera displacement from figure 7. The star represents the experimental equilibria before applying the $n = 6$ RMP, and the triangle is the experimental point after applying the perturbation.

employed in the equilibrium reconstruction. It is clear that case 2, which has two lobes, has the strongest effect, both to stabilize the low-n peeling modes and to drive the higher-n ballooning modes. It is also instructive to compare cases 1 and 3 when only one lobe is present. Case 1 has a more destabilizing effect on the ballooning modes since the lobe is further to the low-field side in the region of unfavourable curvature, exacerbating the ballooning drive, whereas case 3 has the strongest stabilizing effect on the peeling modes since the narrower poloidal extent means that the edge magnetic shear increases further. It is also worth noting that the experimental operating point measured after the RMPs are turned on, i.e. with a much wider pressure pedestal, lies in the high-n ballooning unstable region. If the wider pedestal had been included in the stability analyses (or indeed if lobes with greater radial extent had been simulated), this effect would be further enhanced and the stability boundary would move to even lower normalized pressure.

Next we consider the effect of applying an $n = 6$ RMP. The finite-n peeling–ballooning boundary for the four plasma shapes shown in figure 8(b) is given in figure 15. Consistent with the results presented in figure 12, case D is more destabilizing to ballooning modes and more stabilizing to peeling modes than case A. The addition of extra lobes further amplifies both effects. Case C is more destabilizing to ballooning and more stabilizing to peeling than case B, which in turn has a stronger effect than just one lobe in case A. Furthermore, in keeping with the result in figure 13, the destabilization of the ballooning modes is stronger when there are multiple lobes (as in case B and C) than when there is one more extended lobe (case D).

Figure 2 shows that as well as lobe structures on the low-field side, the RMPs cause similar radially extended long-lasting lobes on the high-field side. If the presence of lobes in the unfavourable curvature region result in ballooning stability degradation, then lobes on the high-field side might be expected to enhance stability as field-lines linger in the good curvature region. However, the addition of ancillary high-field lobes in addition to the low-field side lobes results in negligible change to the mode growth rate. Whilst certain field-lines are more stable, the lobes on the low-field side still allow some field-lines to linger in unfavourable curvature, and this dominates ballooning stability. This was also observed in the systematic study in [12].

Finally, we compare the efficacy of ballooning mode destabilization by lobe structures present when $n = 3$, $n = 4$ and $n = 6$ RMPs are applied in MAST. Figure 16 shows the peeling–ballooning boundaries for plasma shapes most akin to those seen in the visible imaging when RMPs are applied. It is worth noting that in an attempt to most closely match the lobe structure observed in the visible imaging, effectively the achievable shapes result from different applied field strength. For instance, the $n = 3$ plasma boundary is almost identical to that shown in figure 7, since the broad perturbation to the separatrix allows accurate equilibrium reconstruction, whilst the $n = 4, 6$ shapes are less extended than the experimental data, symptomatic with lobes produced when lower in-vessel coil currents are applied. The $n = 4$ shape is case 2 from figure 8(a) and the $n = 6$ shape is case C from figure 8(b). It is evident that at least for the approximations to the shapes employed in this study, the $n = 4$ configuration is the most destabilizing to the ballooning modes and most stabilizing to the peeling modes. One can conclude from the systematic study presented above that the strongest effect from $n = 4$ is due to having a combination of a lobe further on the low-field side than either $n = 3$ or $n = 6$ and importantly having at least two narrow lobes. The $n = 3$ perturbation has least effect since the lobes are more poloidally extended, so do not increase the magnetic shear nor degrade the curvature as much. Of course, the position and poloidal extent of these three-dimensional lobe structures would be different in a different toroidal plane, and so have a subtly different effect on the stability boundary. However, using two shapes derived from applied RMPs with different phases yielded similar destabilization of the ballooning boundary. It is worth reiterating that the axisymmetric treatment employed here forces the poloidal field

in the lobes to become very small, which in turn causes the destabilization of the ballooning modes. A full optimization of the lobe structures for ELM mitigation requires a proper three-dimensional treatment, and is the subject of future work.

6. Conclusions

One potential mechanism to describe how RMPs may cause ELM mitigation is presented. Although the magnetic perturbation causes a reduction in the pedestal pressure gradient, the peeling–ballooning stability boundary is degraded such that the critical pressure gradient to cause an ELM is much lower. This means that ELMs are triggered more frequently despite the reduced pressure gradient. A possible cause of this degradation of stability boundary which is analysed here is the presence of lobe structures near the X-point.

The presence of the lobes helps to drop the pedestal pressure gradient since infinite-n ballooning modes, which at least in MAST represent a good proxy for kinetic ballooning modes [20], are driven more unstable and so enhance pedestal transport. This model may help us to explain why ELM mitigation is most often observed when resonant magnetic perturbations are applied [8–10]. ELM suppression has only been achieved in DIII-D when the RMP is best aligned with the plasma magnetic field [7], and a mis-alignment or a variation from optimal pedestal collisionality leads to an increase in ELM frequency. This is consistent with figure 5, whereby the non-optimized RMP causes a degradation of ballooning stability, but does not incur sufficient heat and particle transport to drop the pressure gradient below the level needed to avoid peeling–ballooning modes.

After the H-mode transition in MAST, it is routinely observed that as the magnetic pressure increases, the ELM behaviour transitions from type-III small ELMs to an ELM-free period, followed by normal type-I ELMs. It has previously been postulated that the effect of RMPs was to drop the effective power across the separatrix with respect to the L-H transition power threshold [9], for instance causing a transition from type-I ELMs to an ELM-free period. However, more recent MAST experiments have demonstrated that the application of RMPs can cause a reliably ELM-free plasma to transition to a type-I ELMing regime when the non-axisymmetric field is applied. This could only happen, despite the drop in the pedestal pressure gradient, if the stability boundary for the peeling–ballooning modes thought to be responsible for type-I ELMs is modified, supporting the model presented above.

ELM suppression has never been achieved in a double-null configuration [9]. It could be postulated that this is symptomatic of the degradation of the ballooning stability presented in this analysis. Since the field-lines exist for most of their length in a region of low poloidal field near the X-point, they are most sensitive to the curvature in this region. When RMPs are applied, the lobe structures will appear near to both X-points, meaning the destabilization afforded by the field-lines existing in the region of unfavourable curvature is exacerbated by the presence of lobes near both X-points.

The strongest ELM mitigation observed in ASDEX Upgrade [8] and JET [50], occurs above a threshold in pedestal density. At higher density the bootstrap current is reduced, lowering the peeling-mode drive and resulting in an increase in the toroidal mode number of the most unstable peeling–ballooning mode. Since the most unstable modes with high pedestal density are primarily ballooning in character, they are even more susceptible to changes in the ballooning stability boundary, possibly explaining why ELM mitigation is optimized in this regime experimentally. The opposite is true of the ELM suppression observed in DIII-D [7], which only occurs at low collisionality, where the bootstrap current is maximum. In this case the peeling character of the mode is strongest, and so the presence of the lobes stabilizing the stability boundary may help us to explain why ELMs are not triggered.

The analysis presented here does, of course, rely upon nested flux surfaces with no magnetic islands or stochastization of the edge field. The fact that field-line tracing calculations predict the observed lobe structures does suggest that this assumption is invalid. Nonetheless, we present the stability implications if the shape of the confined plasma is taken to have a distorted separatrix. These axisymmetric ideal calculations are no doubt a simplification of the experimental situation, but the concepts may help us to understand how ELM control by resonant magnetic perturbation occurs. The primary result of this work is the notion that the resonant magnetic perturbations cause a modification of the peeling–ballooning stability boundary, dropping the critical pressure gradient to a lower value than the reduced pedestal pressure gradient resultant from the RMP-induced enhanced particle transport. The analysis presented here is a first step to quantitatively assessing this new degraded peeling–ballooning boundary. In the future non-ideal equilibria allowing for stochastic fields will be considered, as will the three-dimensional toroidicity of the plasma, both of which no doubt play a role in determining the stability boundary.

Acknowledgments

We thank Dr A.W. Morris, Dr G.T.A. Huysmans, Dr T.C. Hender and Professor H.R. Wilson for helpful discussions. This work was partly funded by the RCUK Energy Programme under grant EP/I501045, the European Communities under the contract of Association between EURATOM and CCFE. The views and opinions expressed herein do not necessarily reflect those of the European Commission.

References

[1] Connor J.W. 1998 *Plasma Phys. Control. Fusion* **40** 531
[2] Snyder P.B. *et al* 2002 *Phys. Plasmas* **9** 2037
[3] Wilson H.R. *et al* 2006 *Plasma Phys. Control Fusion* **48** A71
[4] Suttrop W. 2000 *Plasma Phys. Control Fusion* **42** A1
[5] Loarte A. *et al* 2003 *Plasma Phys. Control Fusion* **45** 1594
[6] Evans T. *et al* 2004 *Phys. Rev. Lett.* **92** 235003
[7] Evans T. *et al* 2008 *Nucl. Fusion* **48** 024002
[8] Suttrop W. *et al* 2011 *Phys. Rev. Lett.* **106** 225004
[9] Kirk A. *et al* 2011 *Plasma Phys. Control Fusion* **53** 065011
[10] Liang Y. *et al* 2010 *Nucl. Fusion* **50** 025013
[11] Snyder P.B. *et al* 2012 *Phys. Plasmas* **19** 056115

[12] Saarelma S. *et al* 2011 *Plasma Phys. Control. Fusion* **53** 085009
[13] Evans T. *et al* 2005 *J Phys: Conf. Ser.* **7** 174
[14] Wingen A. *et al* 2009 *Nucl. Fusion* **49** 055027
[15] Kirk A. *et al* 2012 *Phys. Rev. Lett.* **108** 255003
[16] Saarelma S., Kwon O.J. and Kirk A. 2011 *Plasma Phys. Control. Fusion* **53** 025011
[17] Huysmans G.T.A. 2005 *Plasma Phys. Control. Fusion* **47** 2107
[18] Webster A.J. 2009 *Phys. Plasmas* **16** 012501
[19] Scannell R. *et al* 2012 Edge profiles during ELM mitigation on MAST *Plasma Phys. Control. Fusion* submitted
[20] Dickinson D. *et al* 2011 *Plasma Phys. Control. Fusion* **53** 115010
[21] Huysmans G.T.A., Goedbloed J.P. and Kener W.O.K. 1991 *Proc. Int. Conf. on Computational Physics (Amsterdam, Holland, 1991)* (Singapore: World Scientific) p 371
[22] Wilson H.R., Snyder P.B., Huysmans G.T.A. and Miller R.L. 2002 *Phys. Plasmas* **9** 1277
[23] Saarelma S. *et al* 2009 *Plasma Phys. Control. Fusion* **51** 035001
[24] Sauter O., Angioni C. and Lin-Liu Y.R. 1999 *Phys. Plasmas* **6** 2834
[25] Sauter O., Angioni C. and Lin-Liu Y.R. 2002 *Phys. Plasmas* **9** 5140
[26] Liu Y.Q., Sun Y. and Kirk A. 2012 Toroidal modeling of penetration of the resonant magnetic perturbation field *Phys. Plamsas* submitted
[27] Rozhansky V. *et al* 2011 *Nucl. Fusion* **51** 083009
[28] Tokar M.Z. *et al* 2008 *Phys. Plasmas* **15** 072515
[29] Saarelma S. *et al* 2007 *Plasma Phys. Control. Fusion* **49** 31
[30] Chapman I.T. *et al* 2012 *Plasma Phys. Control. Fusion* **54** 105013
[31] Bird T.M. 2011 The effect of three dimensional shaping on the ballooning stability properties of stellarator equilibria and tokamak equilibria with resonant magnetic perturbations *Thesis* Univeristy of Wisconsin, Madison
[32] Canik J. *et al* 2012 *Nucl. Fusion* **52** 054004
[33] Chapman I.T. *et al* 2010 *Phys. Rev. Lett.* **105** 255002
[34] Jakubowski M.W. *et al* 2009 *Nucl. Fusion* **49** 095013
[35] Nardon E. *et al* 2011 *J. Nucl. Mater.* **415** S914
[36] Cahyna P. *et al* 2011 *J. Nucl. Mater.* **415** S927
[37] Abdullaev S.S. *et al* 2002 *Phys. Plasmas* **15** 042598
[38] Snyder P.B. *et al* 2007 *Nucl. Fusion* **47** 961
[39] Osborne T.H. *et al* 2008 *J. Phys.: Conf. Ser.* **123** 012014
[40] Liu Y.Q. *et al* 2011 *Nucl. Fusion* **51** 083002
[41] Nardon E. *et al* 2007 *J. Nucl. Mater.* **363** 1071
[42] Dickinson D. *et al* 2012 *Phys. Rev. Lett.* **108** 135002
[43] Snyder P.B. *et al* 2009 *Phys. Plasmas* **16** 056118
[44] Snyder P.B. *et al* 2011 *Nucl. Fusion* **51** 103016
[45] Poguste O. and Yurchenko 1986 *Rev. Plasma Phys.* **11** 65
[46] Bishop C.M. *et al* 1984 *Nucl. Fusion* **24** 1579
[47] Bishop C.M. *et al* 1986 *Nucl. Fusion* **26** 1063
[48] Webster A.J. and Gimblett C.G. 2009 *Phys. Rev. Lett.* **102** 035003
[49] Medvedev S.Y. *et al* 2007 *Proc. 34th EPS Conf. on Plasma Physics (Warsaw, Poland)* P4.078 http://epsppd.epfl.ch/Warsaw/pdf/P4_078.pdf
[50] Liang Y. 2012 Private communication Forschungszentrum Jülich